Engineering Anomalously Large Electron Transport in Topological Semimetals

Vincent M. Plisson, Xiaohan Yao, Yaxian Wang,* George Varnavides, Alexey Suslov, David Graf, Eun Sang Choi, Hung-Yu Yang, Yiping Wang, Marisa Romanelli, Grant McNamara, Birender Singh, Gregory T. McCandless, Julia Y. Chan, Prineha Narang, Fazel Tafti, and Kenneth S. Burch*

Anomalous transport of topological semimetals has generated significant interest for applications in optoelectronics, nanoscale devices, and interconnects. Understanding the origin of novel transport is crucial to engineering the desired material properties, yet their orders of magnitude higher transport than single-particle mobilities remain unexplained. This work demonstrates the dramatic mobility enhancements result from phonons primarily returning momentum to electrons due to phonon-electron dominating over phonon–phonon scattering. Proving this idea, proposed by Peierls in 1932, requires tuning electron and phonon dispersions without changing symmetry, topology, or disorder. This is achieved by combining de Haas - van Alphen (dHvA), electron transport, Raman scattering, and first-principles calculations in the topological semimetals MX_2 (M = Nb, Ta and X = Ge, Si). Replacing Ge with Si brings the transport mobilities from an order magnitude larger than single particle ones to nearly balanced. This occurs without changing the crystal structure or topology and with small differences in disorder or Fermi surface. Simultaneously, Raman scattering and first-principles calculations establish phonon–electron dominated scattering only in the MGe_2 compounds. Thus, this study proves that phonon-drag is crucial to the transport properties of topological semimetals and provides insight to engineer these materials further.

1. Introduction

Predictions and observations of novel electronic and optoelectronic responses have generated great interest in topological materials due to their potential for device applications and interconnects.[1–3] The carrier mobility, incorporating the carrier lifetime and effective mass in a semiclassical picture, is thus one of the most crucial aspects for charge and heat conductivity and dissipation in real devices. **Figure 1a** shows the measured single particle and transport mobility of various topological semimetals taken from literature[4,5] as well as our results for $NbGe_2$. The transport mobility is directly determined from the longitudinal and Hall resistance. At the same time, the single particle lifetime and mass are extracted from the field and temperature dependence of the quantum oscillations (see Section Electronic Properties in this article and Quantum Oscillations section of the Supporting Information). One particularly perplexing aspect of the transport
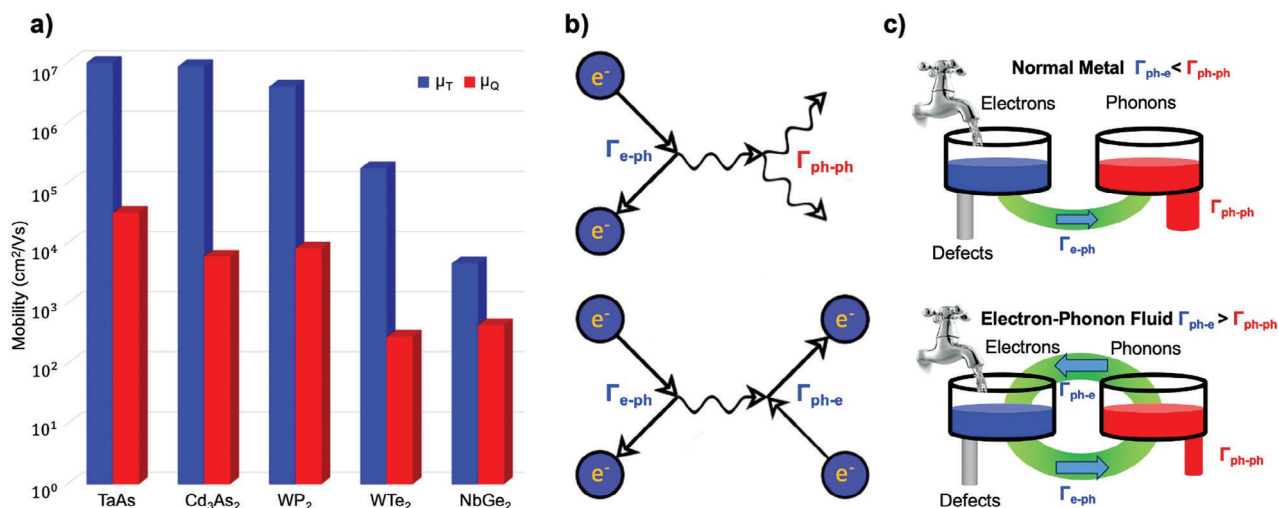
V. M. Plisson, X. Yao, H.-Y. Yang, Y. Wang, M. Romanelli, G. McNamara,
B. Singh, F. Tafti, K. S. Burch
Department of Physics
Boston College
Chestnut Hill, MA USA
E-mail: ks.burch@bc.edu

Y. Wang
Beijing National Laboratory for Condensed Matter Physics
and Institute of Physics
Chinese Academy of Sciences
Beijing 100190, China
E-mail: yaxianw@iphy.ac.cn

G. Varnavides, P. Narang
College of Letters and Science
University of California Los Angeles
Los Angeles, California 90095, USA

A. Suslov, D. Graf, E. S. Choi
National High Magnetic Field Laboratory
Florida State University
Tallahassee, Florida 32310, USA

G. T. McCandless, J. Y. Chan
Department of Chemistry and Biochemisty
Baylor University
Waco, TX 76798, USA

ADVANCED
SCIENCE NEWS
www.advancedsciencenews.com

ADVANCED
MATERIALS
www.advmat.de

Figure 1. a) Measured transport (blue) and single particle (red) mobilities for various topological semimetals.[4,5] Despite significant differences in topology, symmetry, and bulk band structures, these materials exhibit orders of magnitude higher transport than single particle mobilities. b) (top) Scattering diagram for a momentum relaxing scattering event of a single electron in a normal metal. Here, an electron scatters with a phonon, which then scatters with other phonons, dissipating the momentum of the electron into heat. (bottom) Scattering diagram for a momentum-conserving scattering event of a single electron in a phonon-electron fluid. Here, an electron scatters with a phonon, causing it to lose momentum. The phonon then scatters with another electron, effectively returning the momentum of the first electron. c) Cartoon schematic of electron scattering pathways in a normal metal (top) and those in a phonon-electron fluid (bottom). The faucet represents an electric field providing energy and momentum to the electrons. The momentum of these electrons can be lost either by defect scattering or into the phonon bath. From here, anharmonic phonon decay transfers the energy and momentum into heat. However, if the phonon–electron scattering overwhelms the phonon–phonon, the momentum is instead returned to the electron bath, greatly enhancing bulk transport.

in topological semimetals is the three orders of magnitude larger transport (μ_T) mobilities than their single particle (μ_Q) ones. Such enhancements in the transport mobility could pave the way to future low-loss electronic interconnects, but this is currently limited to low temperatures. Thus, there is an urgent need to uncover the origin of these extreme transport mobilities. Some potential explanations have been proposed, ranging from symmetry, topological protection, and chirality-protected backscattering.[4] Nonetheless, experiments have not directly demonstrated how a specific material property, when removed, eliminates this behavior.

Such experiments are crucial as the apparent universality of the anomalous transport in semimetals calls into question the previous potential explanations. For example, if the mechanism's origin results from topology, explaining materials such as WP_2 where the Weyl node is over 300 meV below the Fermi surface is challenging. It is also unclear why such a mechanism would work in materials with different quantum geometries, as anomalous transport appears in Dirac (Cd_3As_2), type-I (TaAs), and type-II (WP_2, WTe_2, $NbGe_2$) Weyl semimetals (Figure 1a). Furthermore, these materials possess different crystal structures, symmetries, and Fermi surfaces of widely varying sizes. However, some Raman scattering experiments suggest a common factor in a few of these materials: phonon–electron exceeds the phonon–phonon scattering.[6–11]

Unlike normal metals, this scenario suggests topological semimetals are in the regime of phonon–electron fluids. Specifically, the phonons primarily decay into electron-hole pairs via phonon–electron scattering rather than into the acoustic continuum via phonon–phonon scattering.[6,12] To see how this affects transport, consider the fate of momentum imparted by an elec-

tric field to the electrons. In a normal metal devoid of Umklapp scattering, an electron loses momentum by scattering off a defect or a phonon[13] (top of Figure 1b). The momentum imparted to the phonon is then lost to other phonons via anharmonic phonon–phonon scattering. As such, phonon-scattering is typically momentum relaxing, as the electrons lose net momenta via electron–phonon scattering to the phonon bath, which is then dissipated into heat via phonon–phonon scattering (top of Figure 1c). However, the phonon can also scatter into another electron (bottom of Figure 1b), giving its momentum to another electron, producing a net momentum-conserving process. As described by Peierls,[14] if the phonon–electron scattering rate (Γ_{ph-e}) is greater than the phonon–phonon one (Γ_{ph-ph}), then the phonons would enhance charge transport by returning the momentum to the electron bath (bottom of Figure 1c). This means a single electron may scatter often, having a reduced single-particle lifetime. However, the momentum-conserving scattering of the phonon–electron fluid nearly cancels the resistive contribution of phonons, enhancing the measured transport mobility. Such a mechanism was proposed to explain the resistivity of some simple metals;[15–17] however, the phonon lifetimes and scattering mechanisms were never directly probed. Indeed, to properly investigate this possibility, one needs to measure the phonon scattering while systematically tuning the phonon–phonon or phonon–electron joint density of states. This must be done without large changes in the system's disorder or affecting its topology and symmetry. This has proven to be a significant challenge. For example, efforts focused on germanium and silicon alloys to tune between dominant phonon–phonon and phonon–electron scattering suffered from large changes in defect scattering.[18,19]

**ADVANCED
SCIENCE NEWS**

www.advancedsciencenews.com

**ADVANCED
MATERIALS**

www.advmat.de
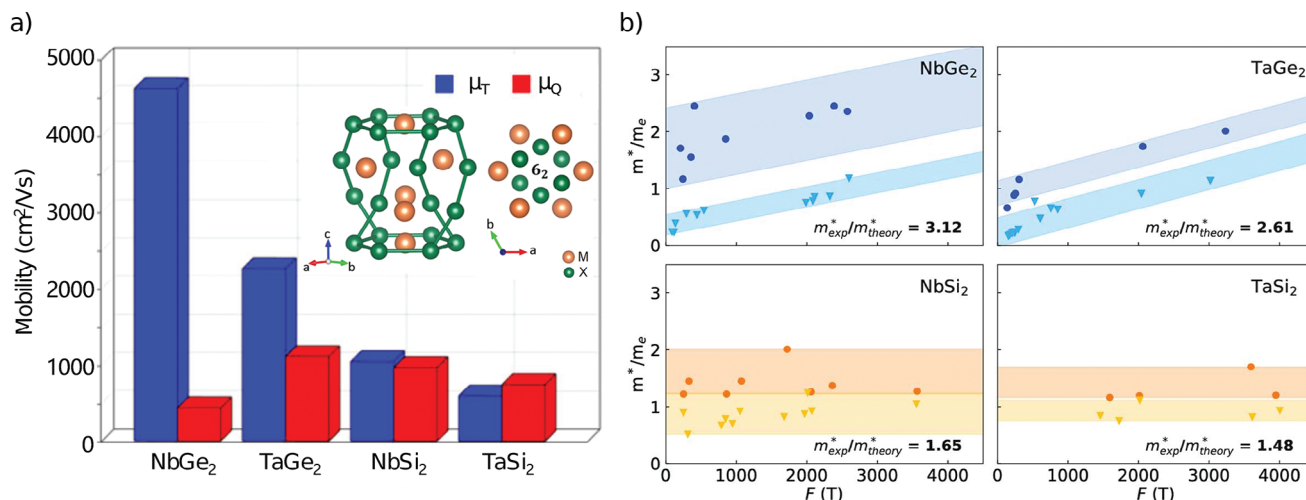
Figure 2. a) Single particle and transport mobility of all four compounds in the MX_2 family. As the series evolves from $NbGe_2$ to $TaSi_2$, a clear trend emerges with the transport mobility (μ_T) decreasing dramatically despite larger single particle mobilities (μ_Q). Inset shows the crystal structure of the MX_2 compounds. b) The experimental (m^*_{exp}) and theoretical (m^*_{theory}) quasiparticle effective masses plotted as a function of dHvA frequencies. A substantial enhancement in the experimental masses over the DFT calculated ones is observed in the MGe_2, but not in the MSi_2. Nonetheless, the overall change in mass between the materials does not explain the trends in mobilities.

The MX_2 family of materials provides a unique solution to test the role of phonon–electron scattering in electron transport with minimal changes in other material properties. Indeed, these materials are established type-II Weyl semimetals, with relatively large transport mobilities and evidence for a phonon-electron fluid in $NbGe_2$.[12,20] Furthermore, recent calculations suggest that phonon–electron coupling differs dramatically between the germanides and silicides.[21] With this in mind, we carefully measured their single particle and transport mobilities. As shown in **Figure 2a**, we find the MGe_2 compounds are similar to other topological semimetals with an order of magnitude difference between μ_T and μ_Q for $NbGe_2$. Upon moving to $TaGe_2$, we observe the transport mobility is reduced by a factor of two, despite the single particle mobility doubling. Nonetheless, $TaGe_2$ has a similar trend to the Nb analog with $\mu_T \gg \mu_Q$, suggesting it is on the border between anomalous and normal metal transport. Upon moving to the MSi_2 compounds, we observe normal metallic transport with nearly equal quantum and transport mobilities. At first glance, this is rather surprising as all four compounds have nearly identical anharmonicity (as determined by phonon frequency shifts shown in Figures S9–S12, Supporting Information), crystal structures, and symmetry shown in the inset of Figure 2a (Space group 180, as determined by X-ray shown in Table S5, Supporting Information). Furthermore, as shown by the good agreement between density functional theory (DFT) calculations and the dHvA measurements discussed later, along with the band dispersions (see Figures S14–S15, Supporting Information) and the topological quantum chemistry database,[22–25] the materials share similar Fermi surfaces and topologies. The dHvA and transport results discussed in the section "Electronic Properties" also indicate similar electronic disorder, consistent with the temperature-dependent X-ray diffraction and Raman linewidth. However, as we reveal through measurements of the phonon scattering rates, Hall resistivity, quantum oscillations, and first-principles calculations of the phonon

self-energies, the change from germanium to silicon results in a switch from phonon–electron to phonon–phonon dominated scattering. This results from subtle changes in the acoustic mode bandwidth and electronic band structure near the Fermi level. We, therefore, provide strong evidence that phonons are at the heart of the remarkable transport behavior in semimetals.

2. Electronic Properties

We began our investigation by determining the electron mobilities for each material. Specifically, transport mobilities were extracted from the longitudinal and Hall resistivities. De Haas - van Alphen (dHvA) experiments were also performed to determine the single particle lifetimes and effective mass, whose ratio is taken to be the single-particle or quantum mobility. Specifically, we studied the dHvA quantum oscillations as a function of magnetic field and temperature to determine the effective mass and quantum lifetime simultaneously (See Section: Quantum Oscillation Data, Supporting Information for details). These experiments allowed us to investigate whether changes in the electronic properties alone can explain the anomalous transport behavior ($\mu_T \gg \mu_Q$), specifically Fermi surface differences, carrier densities, or single particle mobilities (i.e., disorder). The longitudinal and transverse resistivity (ρ_{xx} and ρ_{xy}) were measured from 2 to 300 K with varying the magnetic field from 0 to 9 T. The full data sets at 2 K are shown in Figure S1 (Supporting Information). Due to the established weak anisotropy in the low-temperature transport in these materials,[12,26] we choose to focus on ρ_{xx}, ρ_{xy} and the appropriate dHvA responses. The transport mobility, μ_T, was obtained through a three-band model fit to both ρ_{xx} and ρ_{xy} simultaneously according to the following expressions[27,28]

$$\sigma_{xx}(H) = \frac{\rho_{xx}(H)}{\rho_{xx}^2(H) + \rho_{xy}^2(H)} = \sum_i \frac{\sigma_i}{1 + \mu_i^2 H^2} \qquad (1)$$

**ADVANCED
SCIENCE NEWS**

www.advancedsciencenews.com

**ADVANCED
MATERIALS**

www.advmat.de

$$\sigma_{xy}(H) = \frac{\rho_{xy}(H)}{\rho_{xx}^2(H) + \rho_{xy}^2(H)} = \sum_i \frac{\sigma_i \mu_i H}{1 + \mu_i^2 H^2} \qquad (2)$$

where the conductivity of each band (σ_i) is related to its transport mobility (μ_i) through $\sigma_i = n_i q_i \mu_i$ with $q_i = \pm e$ for a hole or electron band. Adding more bands to the model did not produce additional meaningful information. For the results shown in Figure 2a, we used an average of all μ_i to obtain the transport mobility μ_T for each MX$_2$ compound.

To ascertain the single-particle mobility μ_Q for each MX$_2$ compound, we turned to quantum oscillations probed via dHvA. Here, we measured the magnetic torque in each MX$_2$ sample subjected to a magnetic field from 0 to 41 T at $T = 300$ mK. All four compounds showed rich patterns of oscillations with several frequencies, each corresponding to one branch of the Fermi surface. Using a detailed analysis shown in the Supporting Information (Figures S1 and S2, Supporting Information), we extracted the relaxation time on each Fermi surface τ_j. We then determined the quantum mobility through $\mu_j = q_j \tau_j / m_j^*$ with q_j and m_j^* being the sign and effective mass of carriers on each cyclotron orbit.[29] The individual quantum mobilities for each branch of the Fermi surface are tabulated in Tables S1 through S4 (Supporting Information). Similar to the transport mobility μ_T, the average of these mobilities was taken as μ_Q in the histograms of Figure 2a.

As described earlier, the results of these experiments demonstrate the germanides reveal anomalous transport ($\mu_T \gg \mu_Q$) mobilities, while the silicides have nearly normal metallic responses ($\mu_T \approx \mu_Q$). Thus, we carefully evaluated the quantum oscillation data with density functional theory based first-principles calculations. Specifically in Figure 2b, we plot the experimentally determined and first-principles calculated effective masses versus the dHvA frequencies for each orbit observed. We find excellent agreement between all four materials' calculated and measured frequencies, though there is a discrepancy in the effective masses for the germanides discussed below. As shown in Figure S4 (Supporting Information), while the calculated Fermi surfaces are very similar, there are some slight differences between the silicides and germanides. Specifically, the separate pockets in the first two bands in the silicides are absent in the germanides. However, these small differences cannot consistently explain the trend in the mobilities. The experimentally determined single particle mobilities are relatively similar between TaGe$_2$, NbSi$_2$, and TaSi$_2$. This is in spite of the fact that the transport mobility for TaGe$_2$ is nearly double that found in the silicides. In addition, the μ_Q for NbGe$_2$ is far lower than the rest, yet it possesses a far greater transport mobility. This indicates changes in disorder, and the size of the Fermi surface cannot explain the drastic changes between the germanides and silicides.

Returning to the mobilities, we further investigated the role of the effective mass of the carriers and, thus, the density of states at the Fermi level. Similar to our previous study of NbGe$_2$,[12] we found that TaGe$_2$ also shows an enhancement in the experimentally measured effective mass m_{exp}^* compared with the DFT theoretical values m_{theory}^*. Since these materials possess weak electronic correlations and are non-magnetic, phonon–electron interactions are the prime suspects for the observed mass enhance-

ment. Interestingly, this enhancement is largely suppressed in the silicides, consistent with their transport behavior returning to that of a normal metal.

To see whether the effective masses can explain the electronic transport (μ_T), let us quantitatively examine the differences between the germanides and silicides. Starting with the evolution from NbGe$_2$ to TaGe$_2$, we note a twofold increase in the single particle mobility μ_Q. This occurs alongside a similar size reduction in the effective masses for nearly all orbits. Effective masses nearly half that of NbGe$_2$ are also seen in the silicides. In addition, as mentioned earlier, the silicides reveal nearly identical single particle mobilities as TaGe$_2$. Thus, the changes in single particle mobilities across the MX$_2$ series can primarily be attributed to the effective mass. This is consistent with nearly similar levels of disorder for all four compounds. Nonetheless, the transport mobilities μ_T in MSi$_2$ are also reduced by a factor of two from those found in TaGe$_2$. Taken together, it appears a consistent explanation for the transport and single particle mobilities cannot be found in the disorder or changes in the electronic structure alone. A key takeaway is that the high transport mobilities, which are insensitive to the single particle scattering, also imply dominant forward scattering or processes where the momentum from collisions is returned to the electrons.

3. Phonon Scattering Mechanisms

To explore the role of phonons in the anomalous electronic transport of the MX$_2$ series, we turned to Raman spectroscopy. This tool is excellent for measuring phonon frequencies, linewidths, and symmetries versus temperature. With this information, we can uncover subtle changes in the lattice structure, anharmonicity, and dominant scattering pathways for each material.[30–32] As such, Raman spectroscopy provides a high-resolution probe into the behavior of the optical modes and has already been used to investigate novel states and phonon–electron coupling in topological materials.[6,7,11,33–35] By careful analysis of the temperature dependence of the Raman linewidths, we can determine the decay mechanisms involved for the optical phonons in each compound. Here, we rely on the distinct temperature dependencies of phonon–phonon, defect, and phonon–electron scattering (**Figures 3** and **4a**).

In the case of phonon–phonon scattering, we consider the decay of an optical phonon into two or more acoustic modes, illustrated in Figure 4b. The Klemens model describes the resulting temperature dependence of the linewidth.[36] It is characterized by a monotonically decreasing linewidth with reduced temperature that gives way to low-temperature saturation due to the phonon's Bose statistics. As such, the phonon–phonon decay linewidth (Γ_{ph-ph}) is typically modeled by a Bose-Einstein distribution (n_B) function at half (or one-third) of the frequency of the original mode ω_0 (to account for energy and momentum conservation)

$$\Gamma_{ph-ph}(T) = A\left(1 + 2n_B\left(\omega_0/2, T\right)\right) + B\left(1 + 3n_B(\omega_0/3, T)\right.$$
$$\left. + 3(n_B(\omega_0/3, T))^2\right) \qquad (3)$$
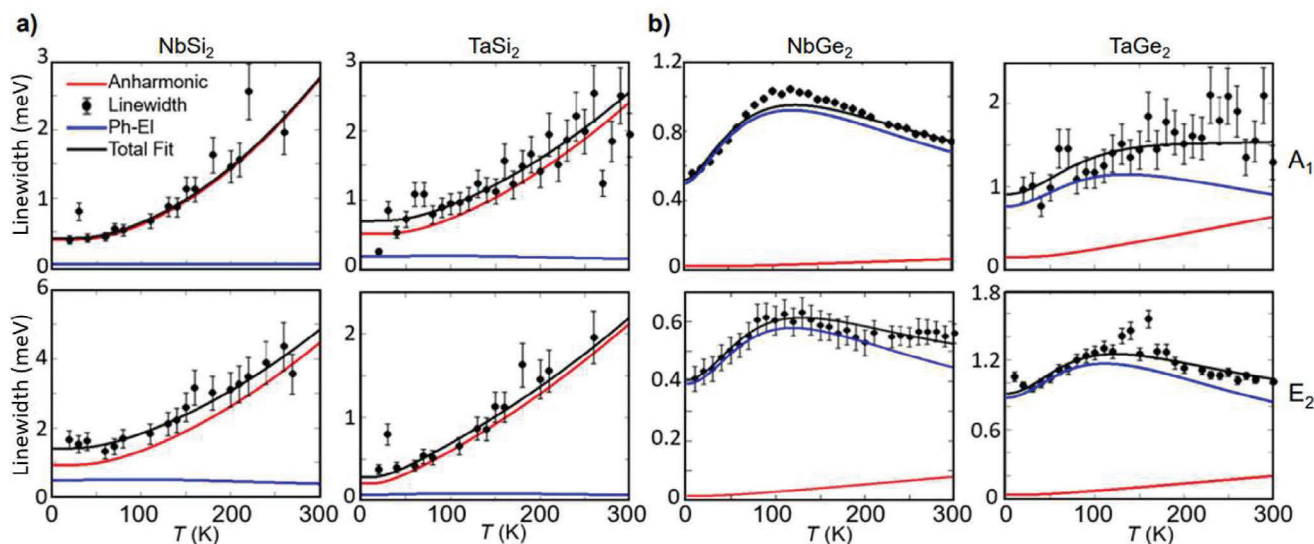
Figure 3. Temperature dependence of the Raman linewidths for A_1 (upper panel) and E_2 (lower panel) modes in a) MSi_2 and b) MGe_2. Measured data are shown in black, the blue curve is a fit to the phonon–electron decay model, while the red curve is the typical anharmonic phonon–phonon contribution. The black line is a sum of both contributions and gives the total fit. We see clear evidence of phonon–phonon dominated linewidths in MSi_2 and phonon–electron dominated linewidths in MGe_2.

To this end, we measured the Raman response of the entire MX_2 family from 10 to 300 K with temperature steps of 10 K. The linewidths versus temperature extracted from fitting the spectra are shown in Figure 3 for representative modes (see the Supporting Information Section for details of the fitting procedures). Focusing first on the MSi_2 compounds shown in Figure 3a, we see nearly temperature-independent linewidths from 10 to 50 K. This is followed by a monotonically increasing linewidth that is approximately tripled by 300 K. This temperature dependence is a typical signature of phonon–phonon scattering and is primarily described by the Klemens model.

A qualitatively different behavior is observed in the MGe_2 compounds (Figure 3b). Here, the linewidths begin to broaden almost immediately with increasing temperature, reaching a maximum value of one and a half to two times larger than the low-temperature linewidths. This is followed by a high-temperature saturation or a decreasing linewidth, sometimes reduced back to its low-temperature value. As the Klemens model of anharmonic
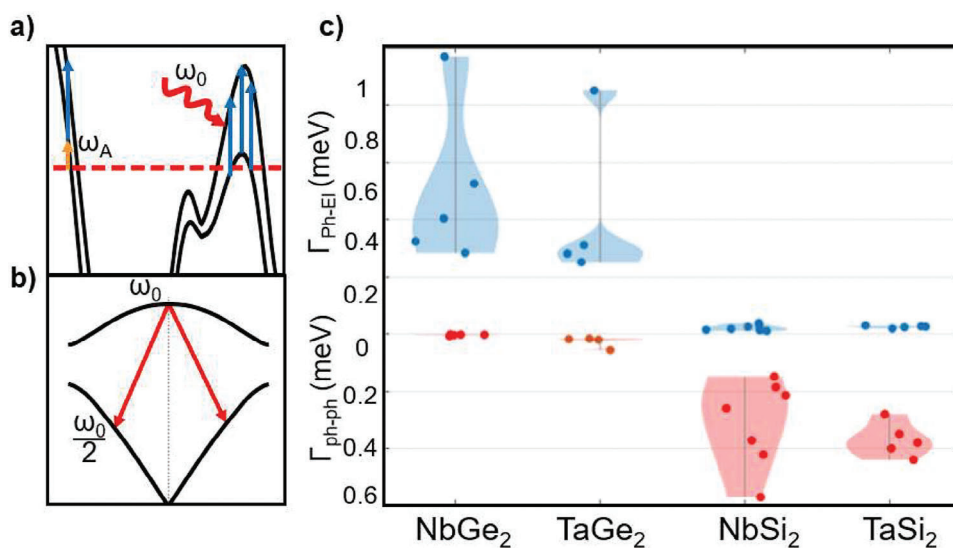
Figure 4. a) Schematic of phonon decay into an electron-hole pair plotted on the band structure of $NbGe_2$. ω_0 is the phonon energy, and the orange arrow is ω_A, the separation of the occupied state from the Fermi level. The blue arrow represents an electron-hole excitation of the same energy as the incident phonon. b) Cartoon schematics of the decay of an optical phonon into a pair of acoustic phonons, conserving energy and momentum. c) Phonon–electron (Γ_{ph-el}) and phonon–phonon (Γ_{ph-ph}) contributions to the Raman linewidths at 10 K of every phonon mode in $NbGe_2$, $TaGe_2$, $NbSi_2$ and $TaSi_2$. The phonon–electron contribution heavily dominates the MGe_2 linewidths, while the phonon–phonon contribution dominates the MSi_2 linewidths.

phonon-phonon decay follows a Bose-Einstein temperature dependence, it fails to explain linewidths that decrease with increasing temperature. This implies that there are scattering pathways other than phonon–phonon decay dominating the phonon linewidths. Indeed, these follow the established pattern of dominant phonon-electron scattering in semimetals.[6,11,12,37] In this case, as illustrated in Figure 4a, the optical phonons decay into an electron-hole excitation (i.e., a pair of Fermions). As such, the probability of scattering is sensitive to the occupation of the initial and final state of the electron involved. We therefore model the temperature dependence of phonon linewidths (Γ_{ph-e}) dominated by phonon–electron scattering by the difference between the Fermi functions (n_F) of the electron and hole following[6,12]

$$\Gamma_{ph-e}(T) = C \int_{-\infty}^{\infty} d\omega_A [n_F(\hbar\omega_A) - n_F(\hbar\omega_A + \hbar\omega_0)]e^{\frac{-(\omega_A-\mu)^2}{2\sigma^2}} \quad (4)$$

here, ω_0 is the low-T phonon energy, and the difference in the two Fermi functions represents the decay into an electron-hole pair. The quantity ω_A represents the separation of the lowest band to the Fermi level. In this work, we added a subtle yet important detail to the model, namely using a Gaussian distribution about ω_A. Simply taking the difference between two Fermi functions implies that there is only one location in the electronic band structure where the optical phonon can decay into an electron-hole excitation. Furthermore, at elevated temperatures, the occupation function usually has a finite smearing factor. By introducing a Gaussian distribution about ω_A and writing the fit as a convolution between this term and the difference in the Fermi functions of the electron and hole, we can account for multiple allowable excitations (Figure 4a) and capture the entire 3D Fermi surface. Indeed, we found this significantly improved our model to more accurately describe the range of temperature-dependent phonon lifetimes we observe. It is important to note that this model still doesn't perfectly capture the anomalous phonon linewidths. Namely, modes for which linewidths decrease with increasing temperature typically show an overshoot at their peak. As one can see in Figure 3b, the A_1 mode of $NbGe_2$ and E_2 mode of $TaGe_2$ both have this feature. One aspect of the model that leads to this is the temperature independence of ω_0 in Equation (4). This assumes that the energy of the phonon is constant. However, as revealed by the frequency shifts shown in Figures S9– S12 (Supporting Information), the phonon energy deviates from ω_0 at finite temperatures. In addition, as we assume a simple Gaussian distribution for ω_A our modeling of the distributions of the initial state of the electron with respect to the Fermi level does not fully capture the true band structure.

Let us now turn to understanding the qualitative nature of phonon–electron-dominated linewidths. Their behavior is explained in the following manner. The initial state must be populated for the electron to be excited to a different band. As the temperature increases, the lower band has a larger thermal population of electrons, leading to an increasing linewidth. Eventually, the states in the upper band begin to get filled while the lower band is emptied. This leads to high-temperature saturation and a decreasing linewidth as the interband transition becomes increasingly Pauli-blocked. As such, the maximum in the phonon–electron scattering rate varies for different modes depending on their energy and the relative electronic states involved (see Figure 3; Figures S5 and S7, Supporting Information). A special case occurs when the initial state of the electron is at the Fermi level. There, at base temperature, the lower band is fully occupied, such that temperature will lower the probability of the phonon–electron decay. This produces a maximum for the linewidths at low temperatures that decreases with increasing temperature, as is seen for the $E_2(4)$ phonon mode in $NbGe_2$.[12]

Before turning to the implications of our findings, we first consider an alternative explanation for the observed anomalous linewidth behavior in the germanides. As shown in the first panel of Figure 3b, below 100 K, it is possible to fit the MGe_2 linewidths to a model of anharmonic decay, as indicated by the black dashed line. This fit would suggest that the Ge compounds have stronger anharmonic scattering than their Si counterparts. This is consistent with what would be expected for a heavier atom. The sudden change in the linewidths in the 100−150 K temperature range might result from a dramatic change in the lattice at these temperatures. However, such a structural change is straightforwardly excluded from our X-ray diffraction and Raman measurements (See Figure S3 and Table S5, Supporting Information).

Alternatively, this effect could result from a dramatic shift in the lattice expansion as a function of temperature. Indeed, such effects have been reported in graphene,[31] although there was no indication that the linewidths deviate from phonon–phonon decay as seen in the germanide compounds (see Supporting Information). Instead, graphene has an inflection point in the energy shifts of the optical phonons due to a negative thermal expansion coefficient. As shown in the supplemental Figures S9– S12 (Supporting Information), we found that in the MGe_2 and MSi_2 compounds, the energy shift of every phonon follows the typical phonon–phonon scattering behavior with no unusual characteristics. We also observe that the magnitude of the shift is nearly the same for all compounds, ranging from 0.2−1 meV, indicating similar anharmonicity for all four compounds. This implies that the behavior of the phonon linewidths does not originate from changes in the lattice. Furthermore, X-ray diffraction data reveal the lattice constants for all four compounds change by at most 0.5% (Table S5, Supporting Information) in this range, decreasing with temperature as expected.

4. Impact of Phonon Dynamics on Transport

To quantify the difference in the dominant phonon scattering mechanism between the compounds, we fit the linewidths to the sum of Equations (3) and (4). This accounts for the possibility of the optical modes decaying into both electrons and phonons. The fits for each mode were obtained by first assuming an additive contribution from both scattering processes. This was based on the general assumption, following Matthiesen's rule, that the contributions from different scattering mechanisms are additive.[38] However, due to their electronic and phononic dispersions, the electron–phonon scattering is expected to have strong momentum dependence.[21] Thus, in the phonon drag regime, the phonon linewidths may not be a manifestation of the direct summation of scattering strength.[38]

**ADVANCED
SCIENCE NEWS**

www.advancedsciencenews.com

**ADVANCED
MATERIALS**

www.advmat.de
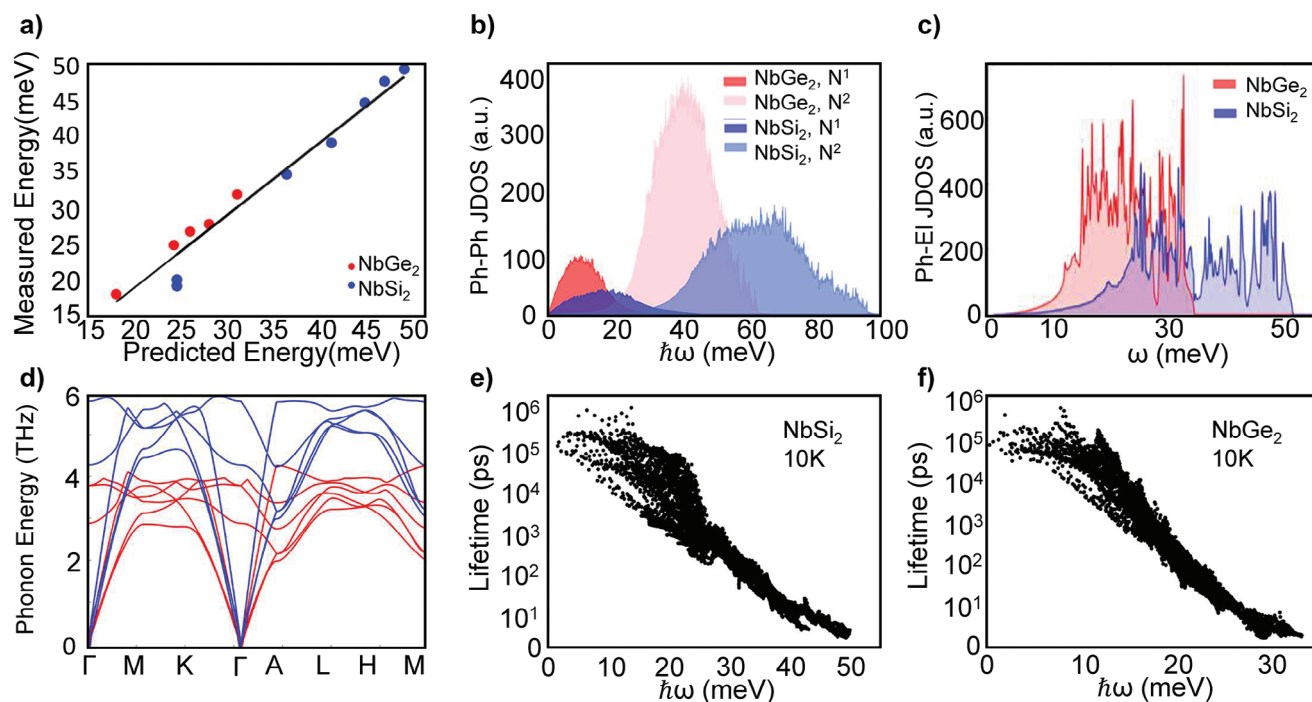
Figure 5. a) Calculated versus measured phonon frequencies for NbGe$_2$ and NbSi$_2$. The black line indicates the ideal agreement. b) Phonon–phonon joint density of states (JDOS) for NbGe$_2$ and NbSi$_2$ which show nearly equal spectral weight despite reduced acoustic bandwidth in NbGe$_2$. c) Phonon–electron JDOS for NbGe$_2$ and NbSi$_2$ which shows approximately 20% larger phase space for phonon–electron decay in NbGe$_2$ than NbSi$_2$. d) Phonon dispersions of NbGe$_2$ and NbSi$_2$ are shown in red and blue, respectively, showing approximately double the acoustic bandwidth for NbSi$_2$ than NbGe$_2$. e,f) Calculated phonon–phonon lifetimes at 10 K for NbGe$_2$ and NbSi$_2$, respectively.

Knowing this, we still choose to be conservative in our estimation of the scattering rates and assume that linewidths showing characteristics of phonon–electron decay had as large of a contribution as possible from phonon-phonon scattering and vice-versa. That is to say, for the germanides, we first start by fitting to the Klemens model and gradually reduce the amount of phonon–phonon scattering as we increase the contribution from the phonon–electron coupling. We followed the same process for modes that show typical phonon–phonon decay behavior but in the opposite direction. This analysis allows us to determine the dominant scattering pathway for each mode without assuming that there is only one decay process at play, and was done for every resolvable phonon mode in each material.

The value of Γ_{ph-ph} and Γ_{ph-e} at 10K from our fits are summarized in Figure 4c. Here, we plot the low-temperature Raman linewidths of all four of the MX$_2$ compounds with the contribution from phonon–electron scattering in the top half of the plot and the phonon–phonon scattering contribution in the lower half of the plot. We focus on the low-temperature values as these are consistent with the temperature at which the mobilities are measured. Similar trends are seen at higher temperatures (see Figure S13, Supporting Information).

It is important to note that this is not a plot of phonon–phonon or phonon–electron scattering strength but instead shows how much each scattering mechanism contributes to the total linewidth of the phonons. In particular, since the phonon–electron scattering in MGe$_2$ is expected to be strongly momentum-dependent,[21] large deviations in Matthiesen's rule are expected. Specifically, rather than different scattering contri-

butions being additive, the total scattering rate is instead dominated by the primary scattering mechanism.[38] This is directly seen in the Raman data summarized in Figure 4c, where the dominance of momentum-dependent phonon–electron scattering leads to the germanide linewidths appearing to only have contributions from phonon–electron scattering.

To confirm this assertion, we turn to our first-principles calculations of the phonon–phonon scattering, indicating that the germanides and silicides have nearly equal strength of phonon–phonon scattering (see: **Figure 5e,f**). Turning to the silicide linewidths summarized in Figure 4c, we see that they are now dominated by phonon–phonon scattering. Unlike the germanides, this is not because of a violation of Matthiesen's rule, but rather due to the phonon-electron scattering being significantly weaker than phonon–phonon scattering. To ensure the accuracy of our results, we have also performed EPW electron–phonon coupling using Wannier functions calculations for NbGe$_2$ and NbSi$_2$, which are consistent with the NbGe$_2$ linewidths being dominated by phonon–electron scattering. In contrast, the calculations show the NbSi$_2$ linewidths are dominated by phonon–phonon scattering, primarily due to much weaker phonon–electron scattering. Details of these calculations can be found in the Supporting Information).

Having established the nature of the phonon scattering in the MX$_2$ family, we now attempt to correlate the phonon scattering with the anomalous transport in NbGe$_2$ and TaGe$_2$. From the Raman (Figure 4c) and transport (Figure 1a) data for the MX$_2$ family, we see the phonon–electron fluid vanishing as the material is tuned from germanium to silicon. Raman linewidths of

**ADVANCED
SCIENCE NEWS**

www.advancedsciencenews.com

**ADVANCED
MATERIALS**

www.advmat.de

NbGe$_2$ revealed the strongest relative phonon–electron coupling, and correspondingly, it has the largest bulk transport mobility. As we move to TaGe$_2$ we start to see that the phonon–electron fluid is on the verge of disappearing. Indeed, while $\Gamma_{ph-e} > \Gamma_{ph-ph}$, for the average phonon–electron scattering rate across all modes, the ratio is lower in TaGe$_2$ than NbGe$_2$. The phonon–phonon scattering becomes dominant upon replacing the germanium with silicon, and the phonon–electron fluid vanishes. Since the phonons no longer return momentum to the electron bath, the transport mobility is reduced by half an order of magnitude as we return to a normal metal state.

The transport and Raman results clearly reveal a correlation between the dominant phonon–electron scattering and high transport mobility in NbGe$_2$ and TaGe$_2$. This enhancement of transport when phonon–electron rather than phonon–phonon pathways dominate phonon scattering is consistent with the phonon–electron fluid first described by Peierls in 1932.[14] To the best of our knowledge, this is the first direct demonstration that removing only the dominance of phonon–electron scattering results in a dramatic reduction in transport mobilities.

5. Tipping the Balance Between Phonon-Phonon and Phonon-Electron

We now turn to the electron and phonon dispersions to understand the absence of a phonon-electron fluid in the silicides. As discussed earlier, our first-principles calculations are in good agreement with the experimental dHvA results. Furthermore, the electronic band dispersion and Fermi surfaces alone cannot explain the difference in transport between the silicides and germanides. This is consistent with previous works indicating that the MGe$_2$ and MSi$_2$ compounds have similar electronic band dispersion.[21]

To validate our calculations, we first compared our measured phonon energies to those calculated from first principles. The results of this comparison are shown in Figure 5a, where we see a good agreement for NbGe$_2$ and NbSi$_2$. With confidence that the first principles calculation accurately captures these materials, we calculate the acoustic phonon dispersions as the low-temperature phonon-mediated transport is primarily governed by the acoustic phonons. The resulting dispersions are shown in Figure 5d. We find that the acoustic phonons extend to roughly 4 THz (16 meV) in NbGe$_2$, and to 6 THz (25 meV) in NbSi$_2$ due to its lighter group 14 element. We calculated the phase space for both materials to determine if the reduced bandwidth alone is responsible for greater phonon–electron scattering in NbGe$_2$. We start with the phonon–phonon joint density of states (JDOS) and considered two types of scattering events: up conversion and down conversion. Namely, one phonon mode can decay into two lower-frequency branches or interact with another phonon branch and generate a mode with a higher frequency. They are evaluated via:

$$N^1(q,\omega) = \frac{1}{N}\sum_{\lambda\lambda'}\Delta(-q+q'+q'')\left[\delta(\omega+\omega_\lambda'-\omega_\lambda'') - \delta(\omega-\omega_\lambda'+\omega_\lambda'')\right] \quad (5)$$

$$N^2(q,\omega) = \frac{1}{N}\sum_{\lambda\lambda'}\Delta(-q+q'+q'')\delta(\omega-\omega_\lambda'-\omega_\lambda'') \quad (6)$$

here, $\Delta(-q + q' + q'') = 1$ if $-q + q' + q'' = k$ (the reciprocal lattice vector), and otherwise $\Delta(-q + q' + q'') = 0$. Figure 5b shows the JDOS for NbGe$_2$ and NbSi$_2$. Intriguingly, despite the relatively higher acoustic bandwidth in NbSi$_2$ (Figure 5b), we find the integrated JDOS is fairly similar to that of NbGe$_2$. This may result from a phonon continuum in these materials. Indeed, unlike other compounds with an optical gap, the acoustic modes continuously evolve into the optical ones. It is important to note that for any given energy, the JDOS of NbGe$_2$ and NbSi$_2$ are not necessarily equal. This is a very important detail for two reasons: 1) the low-energy acoustic phonons govern transport, and 2) it is the JDOS at the energies relevant to the electronic excitations near the Fermi surface that determine whether the phonons will primarily scatter with other phonons or with electrons. This motivated us to calculate the phonon-electron JDOS to quantify the overlap between the phonon structure and the electronic structure (shown in 5c.) Before discussing this calculation, we first identify the phonon lifetimes resulting from phonon–phonon scattering. The results at 10 K for NbSi$_2$ and NbGe$_2$ are shown in (Figure 5e,f), with the 300 K results shown in the Supporting Information. Consistent with our JDOS calculations, at low energies relevant to low-temperature transport, we find that the phonon–phonon lifetimes for NbGe$_2$ and NbSi$_2$ are nearly equal.

We now turn to calculating the phase space for phonon-electron scattering following

$$N(\omega) = \frac{g_s^2}{N_k N_k'}g(\mu)^2\sum_{k,k',b,b',\alpha}\delta(\hbar\omega - \hbar\omega_{k-k'}^\alpha)\delta(\mu - \varepsilon_k^b)\delta(\mu - \varepsilon_k'^{b}) \quad (7)$$

where $\epsilon_{k,b}$ denotes the electronic state with band index b and wavevector k, ω the phonon frequency with mode index α, and the prefactors are employed for the single-particle DOS renormalization. Figure 5c shows the ph-e scattering phase space for both NbGe$_2$ and NbSi$_2$, as a function of phonon frequency. For both compounds, the scattering phase space for all-optical phonon modes is significant and distributed relatively evenly. Integrating over the phonon frequency yields roughly $\approx20\%$ larger phase space for phonon–electron scattering in NbGe$_2$. This larger phase space for phonon–electron scattering also dramatically reduces phonon lifetimes in NbGe$_2$. Specifically, consistent with previous reports,[21] we find the low energy phonon–electron lifetimes at 300 K in NbGe$_2$ are ≈0.1 ps, whereas in NbSi$_2$ they are ≈10 ps. This should be compared with the phonon–phonon lifetimes for both compounds at 300K (shown in Figure S6, Supporting Information), which are 10 picoseconds. Thus, our calculations show the scattering rates of the acoustic modes have a ratio of $\tau_{ph-el}/\tau_{ph-ph} \approx 10^{-1}$ for NbGe$_2$, while it is nearly unity for NbSi$_2$. We want to emphasize that it is this balance of phonon–phonon versus phonon–electron rates and not the strength of phonon–electron coupling that is responsible for the formation of the phonon–electron fluid. When the system is in a regime where the phonon–electron phase space is larger than the phonon–phonon phase space, the phonon–electron lifetimes are dramatically reduced, and the phonons will primarily scatter with electrons, therefore conserving the momentum of the electron bath and enhancing transport.

Hence, our calculations confirm our experimental findings that phonon–electron scattering dominates in the germanides, while the silicides reside in the normal regime of phonon–phonon scattering. Furthermore, this occurs alongside the change from anomalous to normal metal transport without changes in topology, symmetry, or lattice structure and with nearly similar disorder and Fermi surface. We have, therefore, established that removing the dominant phonon–electron scattering alone results in the removal of anomalous transport mobilities. Hence, phonons are central to the enormous electron transport in topological semimetals. Our study also reveals that the dramatic difference between germanides and silicides cannot easily be attributed to the electronic or phonon properties alone. Indeed, the enhanced phonon–electron scattering in the germanides results from subtle details of both the electronic and phonon dispersions. Specifically, phonon decay into an electronic excitation near the Fermi level is only possible if the phonon energy and momentum match what is needed to excite an electron-hole pair (i.e., kinematic constraints). Here, this overlap appears to be reduced by tuning the orbital extent and mass of the ligand atom (Ge to Si). In particular, our calculations indicate that upon going from silicon to germanium, the increased mass reduces the acoustic phonon bandwidth while the enhanced spin-orbit coupling tunes the Fermi surface. These combine to produce a larger phase space for phonon–electron scattering.

6. Moving Forward

Though the quantum geometry of the electronic structure is not a contributing factor in the MX_2 series, the topological semimetal state appears to be a common host for a coupled phonon–electron fluid. Combining heavy atoms with strong SOC and light atoms with extended orbitals is an established path to create a good topological metal. Along these lines, it seems the main factor that is critical for forming a phonon–electron fluid overlaps with that of topological semimetals and includes both 1) heavy atoms (in this case, to reduce acoustic phonon bandwidth) and 2) a second atom with extended orbitals to optimize the scattering phase space. However, it seems the light atom must be selected carefully to maintain the delicate balance between the phonon and electron dispersions. Indeed, for the MX_2 series, the silicon atom in $TaSi_2$ and $NbSi_2$ still enables a topological semimetal but slightly enhances the phonon–phonon scattering phase space while also dramatically reducing the overlaps in the electronic and lattice dispersions. Since $NbGe_2$ and $TaGe_2$ are already very close to the "tipping point", as soon as the relative phase spaces for scattering invert, the phonon–electron fluid disappears with a dramatic reduction in the transport mobility.

Having an accurate understanding of the origin of the unique transport behavior in topological semimetals allows us to exploit the material properties that bring us into this transport regime. For example, if the acoustic bandwidth can be further reduced or an optical-acoustic gap can open, such as the case in WP_2,[6] this would prevent the growth of phonon–phonon scattering at high temperatures. As such, the phonon–electron fluid, and thus, large transport mobilities, could be extended to higher temperatures. Similarly, given the large difference in the mean free paths between electrons and phonons, it is unclear how the phonon–electron fluid will be modified when these systems are reduced to the nanoscale. Indeed, these materials were shown to be promising candidates for electronic interconnects.[39] The strong enhancement of electron transport via phonons in these materials also suggests the phonon–electron fluid could be exploited via coherent phonon pumping to create novel states of matter.[2,40] Furthermore, a natural conclusion of our work is that the quantum geometry near the Fermi surface is not central to the anomalous transport in topological semimetals. This is a surprising result, especially given recent calculations suggesting quantum geometry is crucial for understanding enhancements in phonon–electron coupling.[21,41] We note that our findings do not necessarily support the conclusion that phonon–electron coupling is largely enhanced in these materials. Rather, the phonon–electron fluid emerges from tipping the balance between phonon–electron and phonon–phonon scattering. As such, the mechanisms proposed may not lead to enhancements in superconductivity or the formation of polarons. There have also been reports that phonons can induce topological transitions in Dirac materials.[42] Nonetheless, further work is needed to see if the intricate interplay between the phonons and electrons in these systems means materials with topological phonons also reveal novel transport behavior.[43,44]

7. Experimental Section

Crystal Growth: Single crystals of MX_2 were synthesized by chemical vapor transport (CVT) technique with iodine as the transport agent. The starting elements were all high-purity powders mixed in stoichiometric ratios with 50 mg of iodine, and sealed in silica tubes under a vacuum. The best conditions was found to make high-quality crystals were to place the tubes inside a box furnace (minimal temperature gradient) and keep it at 900 °C for one month.

Electrical Transport Measurement: Resistivity and Hall effect were measured using a standard four-probe technique using the Quantum Design PPMS Dynacool instrument. The heat capacity was measured using PPMS with a relaxation time method on a piece of poly-crystalline sample cut from sintered pellets.

Quantum Oscillation: Quantum oscillation experiments under continuous fields up to 41 T were performed at the National High Magnetic Field Laboratory in Tallahassee, Florida. A piezo-resistive cantilever technique was used to measure the dHvA effect (Piezo-resistive self-sensing 300 × 100 µm cantilever probe, SCL-Sensor. Tech.). A ^{3}He cryostat was used for high-field experiments at temperatures down to 0.3 K.

Density Functional Theory: Density functional theory (DFT) calculations with the full-potential linearized augmented plane-wave (LAPW) method were implemented in the WIEN2k code[45] using the Perdew-Burke-Ernzerhof (PBE) exchange-correlation functional[46] and spin-orbit coupling (SOC). The basis-size control parameter was set to $RK_{max} = 8.5$, and use 20000 k-points to sample the k-space. The Fermi surface from Xcrysden was obtained, combined with the DFT band structure calculations. The Supercell K-space Extremal Area Finder (SKEAF) program[47] was applied to find dHvA frequencies and effective masses of different Fermi pockets.[28,48]

Raman Scattering: All data was taken from 10 to 300 K using a 532nm laser in a backscattering configuration. For each of the samples that were measured, three spectra were taken at each temperature to allow for the removal of cosmic spikes and the data was averaged to provide a single spectrum for each temperature. To extract the temperature-dependent behavior of the phonons, each phonon mode was fit to a Voigt profile. The resulting energies and linewidths were then fit to our combined models for phonon-electron and anharmonic scattering.

Computational Details: For the weighted joint density of states (JDOS) and refractive index evaluations, separate DFT calculations were carried out using the implementation in JDFTx.[49] Fully relativistic ultrasoft pseudo-potentials[50,51] for the PBEsol exchange-correlation functional[52] were used, as well as a uniform $6 \times 6 \times 8$ k grid for the six-atom standard primitive unit cell, an energy cutoff of 28 Hartrees, Fermi-Dirac smearing with a 0.01 Hartree width, and a $3 \times 3 \times 2$ phonon supercell. Maximally localized Wannier functions[53,54] were similarly obtained to interpolate quantities for Monte Carlo Brillouin zone integration on finer k and q meshes.[55] Each transition contributing to the JDOS at that transition energy was weighted by the factor $n_F(E_{\mathbf{k}, n}, T) - n_F(E_{\mathbf{k}, m}, T)$, where $n_F(E, T)$ was the Fermi-Dirac distribution function, and the transition occurs between energies $E_{\mathbf{k}, n}$ and $E_{\mathbf{k}, m}$ at the momentum $\mathbf{k}$ for two bands indexed by n and m.

Supporting Information

Supporting Information is available from the Wiley Online Library or from the author.

Acknowledgements

Conflict of Interest

The authors declare no conflict of interest.

Author Contributions

X.Y. and Y.W. contributed equally to this work. V.M.P. and X.Y. should be considered joint first author. V.M.P. performed the Raman experiments and analyzed the data. B.S and G.M. assisted in the Raman data collection. M.R. and Y.W. assisted in the setup of the automated low-temperature microscope. F.T., X.Y grew the MX$_2$ crystals. G.T.M. and J.Y.C. performed the temperature-dependent X-ray diffraction experiments. X.Y. performed the Hall measurements and analyzed them along with the Quantum oscillations. A.S., D.G., and E.S.C performed the de Haas - van Alphen measurements. P.N., Y.W., and G.V. performed first-principles calculations. V.M.P and X.Y. wrote the manuscript with the help of K.S.B., F.T., and P.N; and with contributions from authors. K.S.B. conceived and supervised the project.

Data Availability Statement

The data that support the findings of this study are available from the corresponding author upon reasonable request.

Keywords

[1] C.-T. Chen, U. Bajpai, N. A. Lanzillo, C.-H. Hsu, H. Lin, G. Liang, in *2020 IEEE International Electron Devices Meeting (IEDM)*, IEEE, Piscataway, NJ **2020**, pp. 32.4.1–32.4.4.

[2] Q. Ma, A. G. Grushin, K. S. Burch, *Nat. Mater.* **2021**, *20*, 1601.

[3] J. Liu, F. Xia, D. Xiao, F. J. Garcia de Abajo, D. Sun, *Nat. Mater.* **2020**, *19*, 830.

[4] J. Hu, S.-Y. Xu, N. Ni, Z. Mao, *Annu. Rev. Mater. Res.* **2019**, *49*, 207.

[5] N. Kumar, Y. Sun, N. Xu, K. Manna, M. Yao, V. Süss, I. Leermakers, O. Young, T. Förster, M. Schmidt, H. Borrmann, B. Yan, U. Zeitler, M. Shi, C. Felser, C. Shekhar, *Nat. Commun.* **2017**, *8*, 1642.

[6] G. B. Osterhoudt, Y. Wang, C. A. C. Garcia, V. M. Plisson, J. Gooth, C. Felser, P. Narang, K. S. Burch, *Phys. Rev. X* **2021**, *11*, 011017.

[7] D. Wulferding, P. Lemmens, F. Büscher, D. Schmeltzer, C. Felser, C. Shekhar, *Phys. Rev. B* **2020**, *102*, 075116.

[8] J. Coulter, R. Sundararaman, P. Narang, *Phys. Rev. B* **2018**, *98*, 115130.

[9] F. Jin, X. Ma, P. Guo, C. Yi, L. Wang, Y. Wang, Q. Yu, J. Sheng, A. Zhang, J. Ji, Y. Tian, K. Liu, Y. Shi, T. Xia, Q. Zhang, *Phys. Rev. B* **2016**, *94*, 094302.

[10] J. Joshi, I. R. Stone, R. Beams, S. Krylyuk, I. Kalish, A. V. Davydov, P. M. Vora, *Appl. Phys. Lett.* **2016**, *109*, 3.

[11] A. Sharafeev, V. Gnezdilov, R. Sankar, F. C. Chou, P. Lemmens, *Phys. Rev. B* **2017**, *95*, 235148.

[12] H.-Y. Yang, X. Yao, V. Plisson, K. S. Burch, F. Tafti, *Nat. Commun.* **2021**, *12*, 5292.

[13] X. Huang, A. Lucas, *Phys. Rev. B* **2021**, *103*, 155128.

[14] R. Peierls, *Ann. Phys.* **1932**, *404*, 154.

[15] N. Wiser, *Phys. Rev.* **1966**, *143*, 393.

[16] M. Danino, M. Kaveh, N. Wiser, *J. Phys. F: Metal Phys.* **1981**, *11*, 2563.

[17] T. Takayama, A. Yaresko, A. Gibbs, K. Ishii, D. Kukusta, H. Takagi, *Phys. Rev. Mater.* **2020**, *4*, 075002.

[18] C. Bhandari, D. Rowe, *Contemp. Phys.* **1980**, *21*, 219.

[19] M. Settipalli, V. S. Proshchenko, S. Neogi, *J. Mater. Chem. C* **2022**, *10*, 7525.

[20] E. Emmanouilidou, S. Mardanya, J. Xing, P. V. S. Reddy, A. Agarwal, T.-R. Chang, N. Ni, *Phys. Rev. B* **2020**, *102*, 235144.

[21] C. A. C. Garcia, D. M. Nenno, G. Varnavides, P. Narang, *Phys. Rev. Mater.* **2021**, *5*, L091202.

[22] T. M. Database, Topological materials database, https://topologicalquantumchemistry.org (accessed: January 2024).

[23] B. Bradlyn, L. Elcoro, J. Cano, M. G. Vergniory, Z. Wang, C. Felser, M. I. Aroyo, B. A. Bernevig, *Nature* **2017**, *547*, 298.

[24] M. Vergniory, L. Elcoro, C. Felser, N. Regnault, B. Bernevig, Z. Wang, The (high quality) topological materials in the world, *arXiv preprint arXiv:1807.10271* .

[25] M. G. Vergniory, B. J. Wieder, L. Elcoro, S. S. Parkin, C. Felser, B. A. Bernevig, N. Regnault, *Science* **2022**, *376*, eabg9094.

[26] U. Gottlieb, O. Laborde, O. Thomas, A. Rouault, J. Senateur, R. Madar, *Appl. Surf. Sci.* **1991**, *53*, 247.

[27] X. Yao, J. Gaudet, R. Verma, D. E. Graf, H.-Y. Yang, F. Bahrami, R. Zhang, A. A. Aczel, S. Subedi, D. H. Torchinsky, J. Sun, A. Bansil, S.-M. Huang, B. Singh, P. Blaha, P. Nikolic, F. Tafti, *Phys. Rev. X* **2023**, *13*, 011035.

[28] H.-Y. Yang, T. Nummy, H. Li, S. Jaszewski, M. Abramchuk, D. S. Dessau, F. Tafti, *Phys. Rev. B* **2017**, *96*, 235128.

[29] J. Gaudet, H.-Y. Yang, S. Baidya, B. Lu, G. Xu, Y. Zhao, J. A. Rodriguez-Rivera, C. M. Hoffmann, D. E. Graf, D. H. Torchinsky, P. Nikolic, D. Vanderbilt, F. Tafti, C. L. Broholm, *Nat. Mater.* **2021**, *20*, 1650.

[30] Y. Tian, S. Jia, R. J. Cava, R. Zhong, J. Schneeloch, G. Gu, K. S. Burch, *Phys. Rev. B* **2017**, *95*, 094104.

[31] D. Yoon, Y.-W. Son, H. Cheong, *Nano Lett.* **2011**, *11*, 3227.

[32] E. Riccardi, O. Kashuba, M. Cazayous, M.-A. Méasson, A. Sacuto, Y. Gallais, *Phys. Rev. Mater.* **2019**, *3*, 014002.

[33] A. Zhang, X. Ma, C. Liu, R. Lou, Y. Wang, Q. Yu, Y. Wang, T.-l. Xia, S. Wang, L. Zhang, X. Wang, C. Chen, Q. Zhang, *Phys. Rev. B* **2019**, *100*, 201107.

[34] I. A. Shojaei, S. Pournia, C. Le, B. R. Ortiz, G. Jnawali, F.-C. Zhang, S. D. Wilson, H. E. Jackson, L. M. Smith, *Sci. Rep.* **2021**, *11*, 8155.

[35] Y. Wang, I. Petrides, G. McNamara, M. M. Hosen, S. Lei, Y.-C. Wu, J. L. Hart, H. Lv, J. Yan, D. Xiao, J. J. Cha, P. Narang, L. M. Schoop, K. S. Burch, *Nature* **2022**, *606*, 896.

[36] Y.-J. Han, P. Klemens, *Phys. Rev. B* **1993**, *48*, 6033.

[37] B. Xu, Y. M. Dai, L. X. Zhao, K. Wang, R. Yang, W. Zhang, J. Y. Liu, H. Xiao, G. Chen, S. A. Trugman, J.-X. Zhu, A. J. Taylor, D. A. Yarotski, R. P. Prasankumar, X. G. Qiu, *Nat. Commun.* **2017**, *8*, 14933.

[38] J. M. Ziman, Electrons and Phonons: the Theory of Transport Phenomena in Solids (*Oxford University Press, Oxford, U.K*). **1960**.

[39] D. Gall, J. J. Cha, Z. Chen, H.-J. Han, C. Hinkle, J. A. Robinson, R. Sundararaman, R. Torsi, *MRS Bull. 46, 959-966* (**2021**).

[40] A. S. Disa, T. F. Nova, A. Cavalleri, *Nat. Phys.* **2021**, *17*, 1087.

[41] J. Yu, C. J. Ciccarino, R. Bianco, I. Errea, P. Narang, B. A. Bernevig, *Nontrivial quantum geometry and the strength of electron-phonon coupling*, **2023**. arXiv: 2305. 02340.

[42] I. Garate, *Phys. Rev. Lett.* **2013**, *110*, 046402.

[43] Y. Xu, M. G. Vergniory, D.-S. Ma, J. L. Mañes, Z.-D. Song, B. A. Bernevig, N. Regnault, L. Elcoro, *Catalogue of topological phonon materials*, **2022**. arXiv: 2211.11776.

[44] F. Nathan, I. Martin, G. Refael, *Phys. Rev. Res.* **2022**, *4*, 043060.

[45] P. Blaha, K. Schwarz, F. Tran, R. Laskowski, G. K. H. Madsen, L. D. Marks, *J. Chem. Phys.* **2020**, *152*, 074101.

[46] J. P. Perdew, K. Burke, M. Ernzerhof, *Phys. Rev. Lett.* **1996**, *77*, 3865.

[47] P. Rourke, S. Julian, *Comput. Phys. Commun.* **2012**, *183*, 324.

[48] D. Shoenberg, *Magnetic Oscillations in Metals*, Cambridge Monographs on Physics, Cambridge University Press, Cambridge **2009**.

[49] R. Sundararaman, K. Letchworth-Weaver, K. A. Schwarz, D. Gunceler, Y. Ozhabes, T. Arias, *SoftwareX* **2017**, *6*, 278.

[50] A. Dal Corso, *Comput. Mater. Sci.* **2014**, *95*, 337.

[51] A. M. Rappe, K. M. Rabe, E. Kaxiras, J. Joannopoulos, *Phys. Rev. B* **1990**, *41*, 1227.

[52] J. P. Perdew, V. N. Staroverov, J. Tao, G. E. Scuseria, *Phys. Rev. A* **2008**, *78*, 052513.

[53] N. Marzari, D. Vanderbilt, *Phys. Rev. B* **1997**, *56*, 12847.

[54] I. Souza, N. Marzari, D. Vanderbilt, *Phys. Rev. B* **2001**, *65*, 035109.

[55] F. Giustino, M. L. Cohen, S. G. Louie, *Phys. Rev. B* **2007**, *76*, 165108.